

Abstract

blid bla asdfjwaejhafiauwefawghaweüojawrgjaw

Kurzfassung

Contents

1	Introduction	1
2	Theory	3
2.1	Interaction of X-rays with matter	3
2.1.1	Complex refraction-index	3
2.1.2	Attenuation	4
2.1.3	Refraction	5
2.2	Phase contrast imaging	6
2.2.1	Wave-Front propagation	6
2.2.2	Talbot effect	7
2.2.3	Grating interferometer	8
2.2.4	Grating Types	9
2.2.5	Coherence requirements	10
2.2.6	Visibility and Phase stepping routine	12
2.2.7	Magnification in curved wave geometry	17
2.2.8	Induced uncertainty by an expanded edge thickness at different magnifications	18
2.3	Spatial system response	21
2.3.1	Real- and frequency-space response functions	21
2.3.2	Edge- and Line- spread function (ESF/LSF)	22
2.3.3	PSF of a complex system	23
3	The Setup	25
3.1	The source	26
3.1.1	Dimensions and structure	26
3.1.2	properties	27
3.2	Sample handling between the gratings	28
3.3	detector properties	29
4	Time- and power- stability of the X-ray tube	31
4.1	Time-stability	31
4.1.1	Comparison of the stability over different time periods	31
4.2	Power-stability	31
5	Characterization of the spatial system response	33

6 Spectra measurements	35
7 Comparison of different grating interferometer constellations	37
8 summary and outlook	39
List of Figures	40
List of Tables	40
Acronyms	41
Bibliography	43

1 Introduction

2 Theory

As the focus of this thesis lies on the experimental characterization of the whole setup, but especially on the source properties and the interferometric parts, the underlying theory of the physical principles of this work are presented restricted on the most essential basics.

The interested reader is referred for a further detailed overview about the topic to the recommendations at the beginning of each section, respectively.

2.1 Interaction of X-rays with matter

The region for X-ray radiation lies in between the extreme ultraviolet and the gamma rays in the electromagnetic spectrum, whereby the corresponding photon energies range from approximately 100 eV up to few hundred keV.

Since the discovery of X-rays by Wilhelm Conrad Roentgen in 1895, several ways generating X-rays are developed and still in progress to improve them. The most valuable possibility for scientific application is the generation via Synchrotron radiation. Thereby electrons are forced on a circular orbit with constant energy by strong magnetic fields in a storage ring. Circulating around the circle they emit X-ray radiation at a very narrow bandwidth, corresponding on the energy they were at the beginning forced to.

Producing X-rays for clinical applications a conventional X-ray source is used in general. In this case the radiation is produced by electrons emitted by a heated cathode and then accelerated to the anode. Impacting the anode also called target, the electrons are decelerated and emit thereby a broad spectrum of X-rays known as *Bremsstrahlung*, with characteristic peaks depending on the anode material, respectively. Detailed description about X-ray sources and the interaction of X-rays with matter can be found in [1, 23]. The dependency between the energy and the resulting wavelength is given by the equation:

$$\lambda [\text{\AA}] = \frac{hc}{E} = \frac{12.398}{E [\text{keV}]} \quad (2.1)$$

So the wavelength of X-rays ranges from $12.4 \times 10^{-10} \text{ m}$ for 100 eV down to $0.775 \times 10^{-11} \text{ m}$ for 160 keV, whereby in the region of few 100 eV from soft X-rays, in the hundred keV region of hard X-ray is spoken, respectively.

2.1.1 Complex refraction-index

In analogy to visible light X-rays are also electromagnetic waves, thus in analogy their behaviour passing through any matter can be described by a complex index of refraction

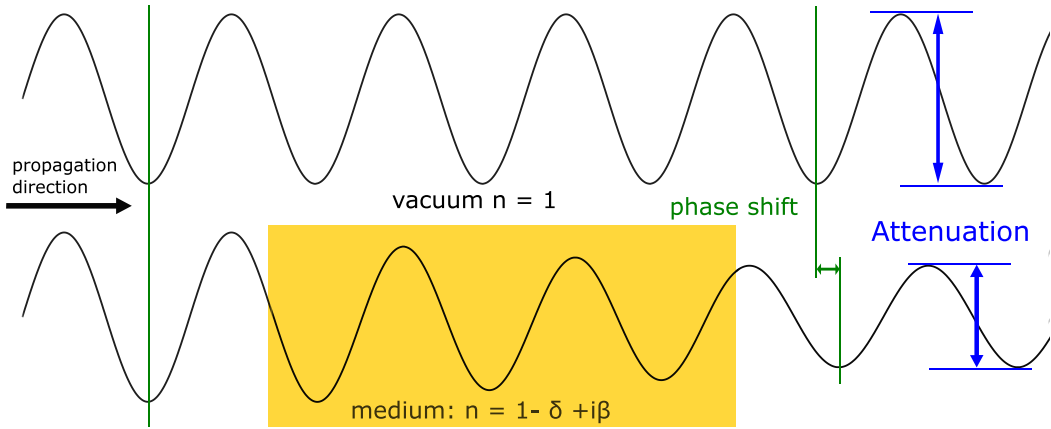


Figure 2.1: Drawing of two electromagnetic waves. The one above propagates in vacuum, the lower wave propagates through a medium with a complex refraction index and thus has a attenuated amplitude and a shifted phase compared to the wave propagation in vacuum. The attenuation is depicted as blue, the phase shift as green arrow, respectively.

[1]:

$$n = 1 - \delta + i\beta. \quad (2.2)$$

Hereby the two constants δ and β depend on the material properties of the passed medium and the energy of the X-rays. The strength of contribution of these two constants can be shown by comparing a wave passing through an arbitrary medium, with constant refractive index n and a wave propagating in vacuum $n = 1$. The most simple way describing such an example, is assuming a plane monochromatic wave without polarization with a propagation orientation perpendicular to the medium's surface as shown in Figure:2.1. These waves are also called scalar wave functions and for $n = 1$ described by:

$$\Psi(z) = E_0 e^{ikz}. \quad (2.3)$$

This equation changes inside the medium to:

$$\Psi(z) = E_0 e^{inkz} = E_0 e^{(1-\delta+i\beta)ikz} = E_0 e^{(1-\delta)ikz} e^{-\beta kz}. \quad (2.4)$$

Here δkz describes the phase shift and $e^{-\beta kz}$ the exponential loss of the amplitude equivalent to the wave's intensity within the medium. The macroscopic effects of these two constants are discussed separately in the following.

2.1.2 Attenuation

Speaking of attenuation of an electromagnetic wave, always the reduction of the wave-amplitude and thus the loss of intensity is meant. This macroscopic attenuation is, over a

broad energy range, dominated by two main effects, known as *photoelectric absorption*, which is an coherent and elastic process, and *Compton scattering* an incoherent and inelastic process, respectively [1]. According to the *Lambert-Beer Law*, the relation between the reduction of intensity and the imaginary part of the refraction index of an object is given by:

$$I = I_0 e^{-2\beta kd} = I_0 e^{-\mu d}, \quad (2.5)$$

with the linear attenuation coefficient $\mu = 4\pi\beta/\lambda$ and I_0 the initial intensity of the wave passing through the object [5]. Obviously μ is dependent of the incoming wavelength, thus the corresponding X-ray energy, and the composition of the illuminated material. So it is perspicuous, that formation of images in attenuation based X-ray imaging is a measure of the material dependent attenuation coefficients and so the intensity loss of the X-ray beam after propagating through the different respective materials in the studied object.

2.1.3 Refraction

Considering the term δkz of equation 2.4 over the thickness d of the medium, the total phase shift for a monochromatic electromagnetic wave is given by:

$$\Phi = \delta kd. \quad (2.6)$$

Contemplating an object which has an change in thickness or the refractive index in the direction normal to the wave propagation, the total phase shift changes also. The consequence of this behaviour is a change of the propagation direction of the incoming X-ray beam. In general this angle of refraction α is equivalent to the local gradient of the phase shift in the two directions perpendicular to the direction of incidence - in this case the z-direction- divided by the wave vector $k = 2\pi/\lambda$. For reasons of simplicity the problem is restricted to the x-direction and thus the gradient eases to a simple derivative in x. The corresponding equation for the refraction angle then simplifies to:

$$\alpha = \frac{1}{k} \frac{\partial \Phi(x)}{\partial x}. \quad (2.7)$$

One main difference comparing visible light and X-rays, is the deviation of the refractive index from one. On the one hand for visible light the refractive index can deviate over a wide range from 1, on the other hand for X-rays the deviation is very narrow. Considering the dependencies of the decrement δ of the index of refraction this behaviour becomes easily clear. The material dependent term δ is also strongly depending on the energy of the X-ray beam, and is defined as:

$$\delta = \frac{\lambda^2 r_e n_e}{2\pi}, \quad (2.8)$$

with the classical electron radius $r_e = 2.818 \times 10^{-15}$ m and the electron density n_e of the material. As example for energies above 12.4keV $\equiv \times 10^{-10}$ m δ is of the order of 10^{-6} . This very small effect leads to very small refraction angles, which causes the need

of interferometric methods detecting these effects indirectly. On the elementary particle level, the process of X-ray refraction can be described by the elastic scattering, also known as *Thomson scattering* [1], of the photons at the electrons of the material the wave is passing through. The key for phase contrast imaging declines to the measurement of these changes of the refraction angle, while the X-rays passes through an object. How this technique works explicitly is further explained in the following section.

2.2 Phase contrast imaging

Another very auspicious technique using the power of X-ray radiation is their property getting slightly refracted, as mentioned above. The plurality of different approaches in this field is tremendous, so the focus lies here on the grating-based phase contrast imaging technique, which is mounted on the setup characterized in further detail on the next chapter. This method uses firstly one grating inducing on purpose a phase shift, depending on the grating design the shift is about $\pi/2$ or π , to the incoming wave front and secondly another grating converting the induced phase shift into intensity variations, thus the detection is possible by a simple conventional flat-panel detector, as in use for the most medical applications. For further detail about the other techniques and the topics in this section see: [3, 4, 14, 17, 23, 26, 27].

2.2.1 Wave-Front propagation

In analogy to nature, a common way describing electromagnetic waves simply, is to consider them as wave-fronts. As mentioned above the wave-front of a X-ray wave changes in a sample due to interaction with matter, meaning absorption and refraction. But nevertheless there are also changes induced while propagating through free space, if no vacuum is provided in that area. Normally the detector is right behind the sample thus this effect can be neglected, but in case of phase contrast imaging propagation through free space is important for the application. According to *Huygens principle* a wave-front can be described at any time by the sum of spherical wavelets distributed over the whole wave-front. This leads to the Fresnel diffraction integral (valid in the homonym *Fresnel regime* also near-field regime), which is the integral over the contribution of all these spherical waves:

$$\Psi(x, y, z) = \frac{e^{ikz}}{i\lambda z} \int \int \Psi(x_0, y_0, 0) e^{\frac{ik}{2z}((x-x_0)^2 + (y-y_0)^2)} dx_0 dy_0, \quad (2.9)$$

whereby x_0 and y_0 are the values in the $z = 0$ plane. With this equation it is possible to calculate the wave-front at any time. The propagation itself is considerable as the convolution of the wave function $\Psi(x, y, z)$ at $z = z_0$ and a so called propagator function:

$$h_d = \frac{e^{ikd}}{i\lambda d} e^{\frac{ik(x^2+y^2)}{2d}}, \quad (2.10)$$

where d denotes the travelled distance. With the convolution theorem, stating that the convolution's Fourier transform is simply the product of the Fourier transform of these

two functions, it is possible to propagate the wave-front over a distinct distance by simple multiplication in Fourier space. Thereby is the Fourier space propagator function the Fourier transform of the propagator function in real space, denoted by:

$$\tilde{P}_d(k_x, k_y) = \mathcal{F}(h_d(x, y)) = e^{ikd} e^{\frac{-id(k_x^2 + k_y^2)}{2k}}, \quad (2.11)$$

which can be shown with simple physical considerations [3].

2.2.2 Talbot effect

Using the Fourier space propagator function the forecast of the wave-front at any propagation distance is very facile. In general simple wave functions, like sine or cosine in other words periodic functions, are used describing the behaviour of electromagnetic waves. In that case general evidences about the resulting propagation can be made. That a periodic wave-front repeats itself after a distinct propagation distance was first discovered by Henry Fox Talbot in 1836 and is known as the Talbot distance d_T [22]. In his studies he used visible light and a grating producing a periodic wave-front, but the effect is also valid for the X-ray range. The determination of the Talbot distance where the wave-front repeats, is done by applying the Fourier transform on a simple periodic wave like in equation 2.3. This transform simplifies to a sum because the Fourier transform of a periodic function with period p is discrete, because only integer multiples of the $k_x = 2\pi m/p$ remain. Staying on an easy level of explanation the calculation is shown just for one dimension:

$$\Psi_0(x) = \frac{1}{2\pi} \int \tilde{\Psi}_0(k_x) e^{ik_x x} dk_x = \frac{1}{2\pi} \sum_m \tilde{\Psi}_0(2\pi m/p) e^{\frac{i2\pi xm}{p}} \Delta k_x, \quad (2.12)$$

with $\Delta k_x = 2\pi/p$. Applying this k_x values in the propagator function $\tilde{P}_d(k_x, k_y)$ the distance the wave-front repeats itself, besides a constant phase shift, is given by:

$$d_{T_n} = \frac{2np^2}{\lambda}, \quad (2.13)$$

whereby $n = 1, 2, 3, \dots$ indicates the Talbot-order. Considering an well known wave-function, for example a step-function induced by a periodic grating, so called *Fractional Talbot distances* arise [3]. A general relation for the fractional distances is given by:

$$d_{T_{frac}} = \frac{np^2}{8\lambda}, \quad (2.14)$$

where n again denotes the Talbot order and p the period of the grating. A special case is the one at half the Talbot distance, where the initial wave-front repeats again besides a transversal shift over half a grating period as the left part in figure 2.2 shows. However, at other Talbot fractions high and low intensity patterns arise and this is the area which is of highly interest in grating interferometry focussing on phase contrast imaging. A main problem is the spectrum illuminating the grating, because the exact revival of the

wave-front only appear, if monochromatic waves are used. Otherwise the pattern lute, due to the fact of to less coherence. Thus the Talbot carpet has only bright and dark regions, which can be seen on the right side of figure 2.2. To overcome this behaviour a third grating is put right behind the source, thus producing equally spaced line sources. The exact arrangement of the gratings and their specific requirements are discussed in more detail in the following section.

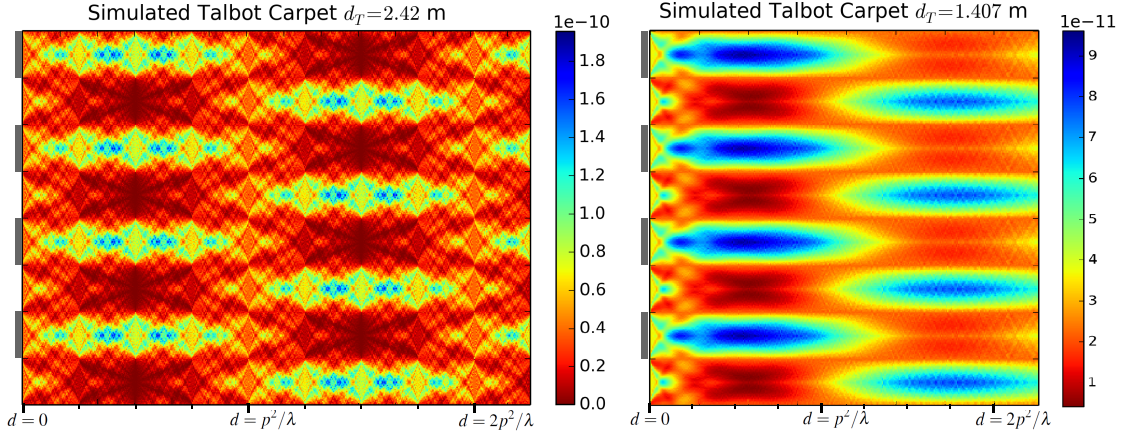


Figure 2.2: *Simulated Talbot-carpets for a gold grating with a duty cycle of 0.5 a phase shift of $\pi/2$ and a grating period of $5\mu\text{m}$. The left one shows a carpet for a monochromatic X-ray source for a energy of 60 kVp , only for this case or a sufficiently coherent source, the return of the initial wave-front pattern at half the Talbot distance and at one Talbot distance can be clearly seen. The right one is for the case of a polychromatic source with its peak-energy at 60 kVp , thus a resulting mean energy of 34.898 kVp . Due to the polychromatic spectrum the patterns are smeared out and the revive of the start wave-front is not possible any-more, just high and low contrast regions are observable.*

2.2.3 Grating interferometer

As mentioned in the sections above the underlying principle of phase contrast imaging is to quantify the refractive index of a sample, or in other words to measure the induced angle of refraction onto the transmitted X-ray wave. The idea behind using a grating interferometer for this method is that a small angular change of the wave-front leads to a transverse shift of the interference pattern induced by the grating. In the optimum case, speaking of a sufficient beam-coherence and a monochromatic spectrum e.g. at synchrotron sources, just two gratings are needed making this technique applicable. Hereby the first grating denoted by G_1 induces the slight shift and the second denoted by G_2 serves as analyser grating detecting the phase shift. Hereby the fluctuations in the phase shift are converted into intensity variations, which can be easily detected by a standard X-ray detector. Thus this works properly, on has to make sure that the analyser

grating is in a position where the interference pattern interferes constructively, otherwise the transmitted intensity will be insufficient. These regions have high visibility, which is explained in further detail in 2.2.6 and can also be seen in figure 2.2 on the left side, at odd fractional Talbot-distances e.g. speaking of $d = p^2/2\lambda$, where the Talbot-carpet has a region of highest contrast. In general applications there is a huge lack between the optimum requirements and the existing properties of source and gratings. Nevertheless there is a way to overcome this problems inducing a third grating right behind the source. This setting, shown in figure 2.3 is known as Talbot-Lau interferometer. At this installation the third grating G_0 , which is an absorption grating, works as a mask for the spacious source, normally used at clinical applications or at labs, with a source size bigger than one square millimetre. This grating slices the source in evenly spaced individually coherent line-sources which interfere with each-other. Installing such a setting, it is important that it full fills the condition:

$$p_0 = p_2 \times \frac{l}{d}, \quad (2.15)$$

thus the individual line-sources interfere constructively and can contribute to the imaging process. Hereby are p_0 and p_2 the respective grating period, l is the distance between G_0 and G_1 and d the distance between G_1 and G_2 . Using this alignment the total source size S is only responsible for the final resolution of the image given by Sd/l and spatial resolution is decoupled from spatial coherence, which allows the use of X-rays with very small coherence length in both directions [17]. A drawing of the geometrical considerations for this conditions above is shown in figure 2.3. As in the further thesis different constellations of gratings will be discussed the next small section focusses on their properties.

2.2.4 Grating Types

In general there are two different grating types, absorption and phase gratings. As one can imaging the main property of absorption gratings is their high absorbency. For that reason the material they are made of has to have high mass thus big Z values e.g. lead or gold. But the toxicity and the very mellow state makes lead infeasible producing gratings with high aspect ratios. Overcoming this problem, absorption gratings are formed using a support layer generally made of silicon, because the handling of Si wavers and their subsequent treatment is well known. The support layer is produced by standard photolithography techniques and its splines are filled afterwards with gold by electroplating mechanism. In the main part of figure 2.4 such an absorption grating with a gold height of $50 \mu\text{m}$ and a grating period of $2.4 \mu\text{m}$ is shown. In general a rule of thumb is the higher the gold filling the better, but as one can imaging forming such high gratings is a very tricky and time extensive process, nevertheless nowadays heights up to $200 \mu\text{m}$ are possible, without bending of the individual grating layers against each other [?]. On the other hand phase gratings usually consist of low Z materials avoiding the effect absorbing radiation, but rather just induce a small angular shift. Due to the fact that these grating type is in no need to absorb the height is way below compared to absorption gratings

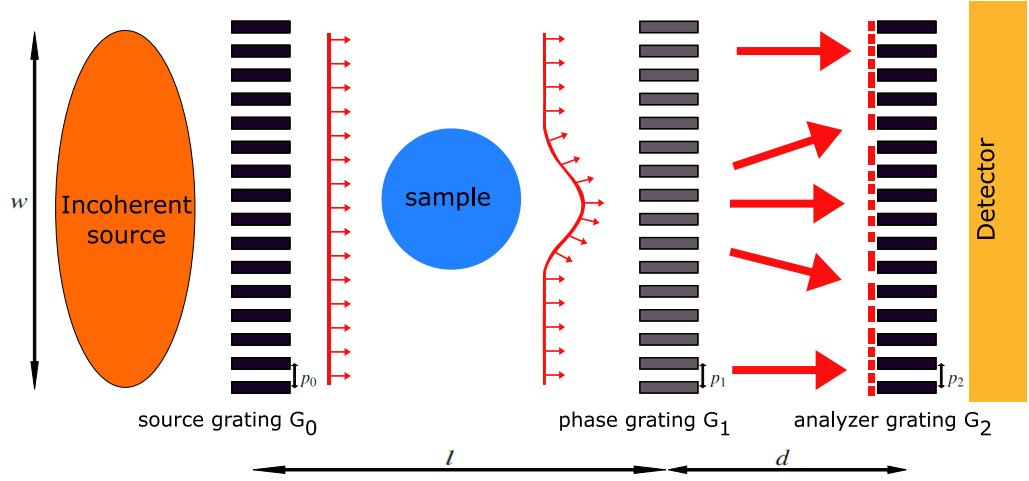


Figure 2.3: Sketch of a Talbot-Lau interferometer. Underlying principle: The source grating G_0 induces individual coherent, but not mutual coherent, line-sources. The sample in the beam slightly refracts each line-source, which yields to a local differential phase gradient accounted due to the intrinsic object properties. This small deviation in the respective propagation direction, maintains to a local variation of the intensity transmitted through the gratings G_1 and G_2 . This variation is then recorded by a standard X-ray detector.

thus no support layer is needed. The inset of figure 2.4 shows such a phase grating made of silicon with a height of $22\ \mu\text{m}$ and a period of $4\ \mu\text{m}$, but there are also various combinations of materials forming such gratings e.g. a silicon grating electroplated with nickel, which is usually used at the setup this thesis is about. For Further reading about production mechanisms and the different grating types see: [?]

2.2.5 Coherence requirements

As mentioned in section 2.2.3 the coherence requirements of the beam can be dropped down to a very low level inducing a third grating (G_0) right behind the source. In this section a short overview about the related formulas and resulting numbers are introduced, getting a feeling about the required dimensions. For further reading see [14, 26]. There are two different coherence types, at one hand longitudinal coherence synonymous to monochromaticity, at the other hand transversal, or spatial coherence is need to be considered. Concerning the longitudinal coherence an approximate expression for the required monochromaticity yielding to good contrast is[27]

$$\frac{\lambda_0}{\Delta\lambda} \gtrsim n \quad (2.16)$$

here λ_0 denotes the design wavelength of the setup, $\Delta\lambda$ the width of the surrounding wavelength and n the order of the Talbot distance from equation 2.13. This expres-

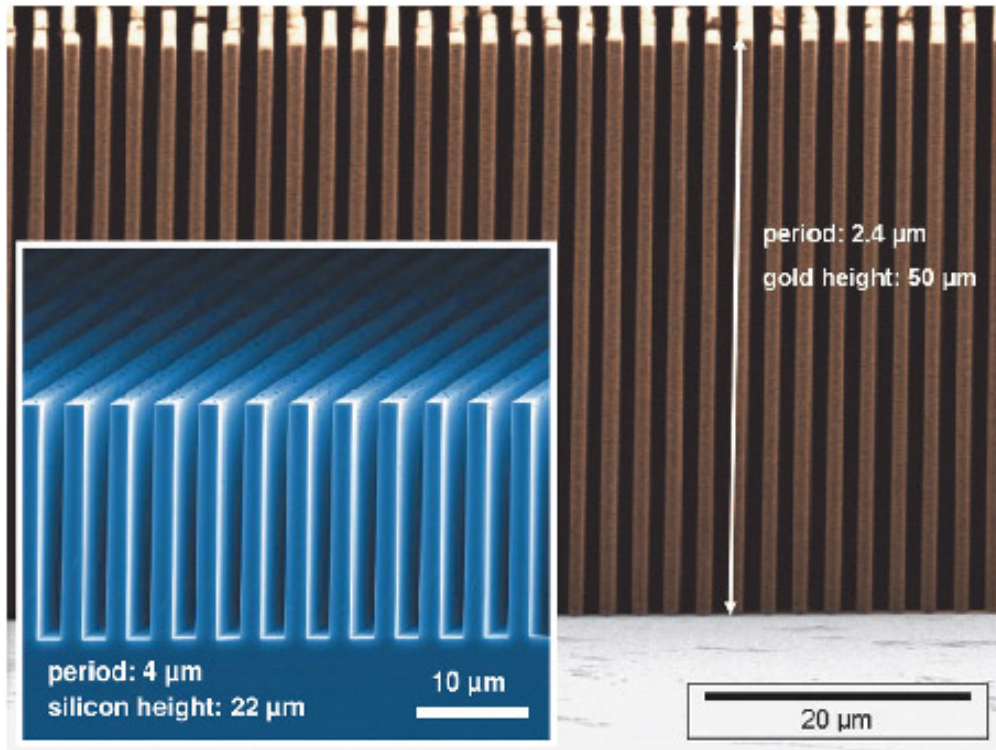


Figure 2.4: *Different types of deep micro-structured gratings used for X-ray grating interferometry, thus phase and/or amplitude modulation is possible, depending on the grating properties, respectively. In the main picture a Gold absorption grating is depicted manufactured at KIT. At the inset a pure Silicon phase grating made at the PSI is shown.* (source: <http://www.esrf.eu/UsersAndScience/Publications/Highlights/2010/imaging/img02>)

sion implies the possibility, applying a polychromatic source for grating interferometry, without loosing significant quality. For that reason, this section focusses more on the spatial coherence requirements, because their influence onto the resulting signal is much higher. As mentioned in section 2.2.3 for the case of considering just plane-waves the final resolution of an image is given by Sd/l . A sketch of this variables is shown in Figure: 2.3, where S is the finite source size, l the distance between G_0 and G_1 and d the distance between G_1 and G_2 , respectively. There are several common definitions for the transversal coherence length ζ_s concurring with each other so here ζ_s is defined as

$$\zeta_s = \frac{\lambda l}{S}, \quad (2.17)$$

where λ is the wavelength corresponding to the design energy the Interferometer is made for. Typical values for an extended source size of about one square centimetre and an

inter-grating distance of about one metre are ζ is $\approx 10^{-8}\text{m}$ and for more advanced micro-focus tubes with much less power or synchrotrons ζ is $\approx 10^{-6}\text{m}$, respectively [17]. A comparison between typical and micro-focus X-ray tubes is given in chapter 3. In the following section a short convulsion of the phase-retrieval mechanism is shown with respect to the coherence requirements depicted in this section.

2.2.6 Visibility and Phase stepping routine

Visibility: The intensity of the fringe pattern right before the analyser grating is modulated by the phase grating, which has an rectangular shape (see Figure 2.4). Just concerning first order diffraction this pattern has nearly as sinusoidal shaped intensity profile. The distance d is adjusted to the fractional Talbot- distances with the highest contrast (see Figure 2.2), where the minima of the intensity pattern drop down to zero for an infinitesimal small source. Using completely coherent radiation, the intensity profile can be expressed by

$$I(x) = I_0 \left(1 + \sin\left(\frac{2\pi x}{p_2}\right)\right), \quad (2.18)$$

thereby x denotes the coordinate transversal to the grating lines, I_0 the intensity before G_1 and p_2 the period of the fringes, whereby the interferometer should be designed in that way, that this period coincides with the analyser grating period. For an expanded source with size s with only partial coherent radiation, the observed intensity pattern changes to a convolution of a point-like source with the projected source profile, with width w . If for simplicity a Gaussian- shaped source is assumed, the convolution results again in a Gaussian with the width

$$w = S \times \frac{d}{l}, \quad (2.19)$$

hereby S and w correlate to the full width at half maximum (FWHM) of the Gaussian, respectively. For the idealized case of an point source the visibility V , which is equivalent to the *Michelson contrast* [?] / is unity, but for real sources speaking of expanded ones like e.g. in Figure 2.3 the visibility drops below unity. The visibility is defined as

$$V = \frac{I_{max} - I_{min}}{I_{max} + I_{min}}, \quad (2.20)$$

whereupon I_{max} and I_{min} denote the maximum and minimum intensity values of the fringe pattern from equation 2.18, respectively. Introducing I_{max} and I_{min} this equation results in:

$$I(x) = \frac{I_{max} + I_{min}}{2} + \frac{I_{max} - I_{min}}{2} \sin\left(\frac{2\pi x}{p_2}\right). \quad (2.21)$$

A analytical investigation of the properties of the convolution of a Gaussian with a sine, yields to an equation for the decrease of the visibility, corresponding to the projected source size w to:

$$V = e^{-(1.887w/p_2)^2}, \quad (2.22)$$

whereas the decrease of V has a Gaussian shape. From this equation it is possible deriving directly an inequality for the projected source size, dependent on the minimum required visibility V_0 and the periodicity p_2 of both the analyser grating G_2 and the intensity pattern, to:

$$w \leq 0.53p_2\sqrt{\ln(V_0)}. \quad (2.23)$$

As one can see in Figure 2.5 the resulting visibility is extremely dependent on the Talbot-distance d_T . As mentioned in section 2.2.2 the highest visibility, independent of dealing with monochromatic or polychromatic radiation, occurs always at fractional Talbot-distances. As the projected source size is also dependent on this effect, due to

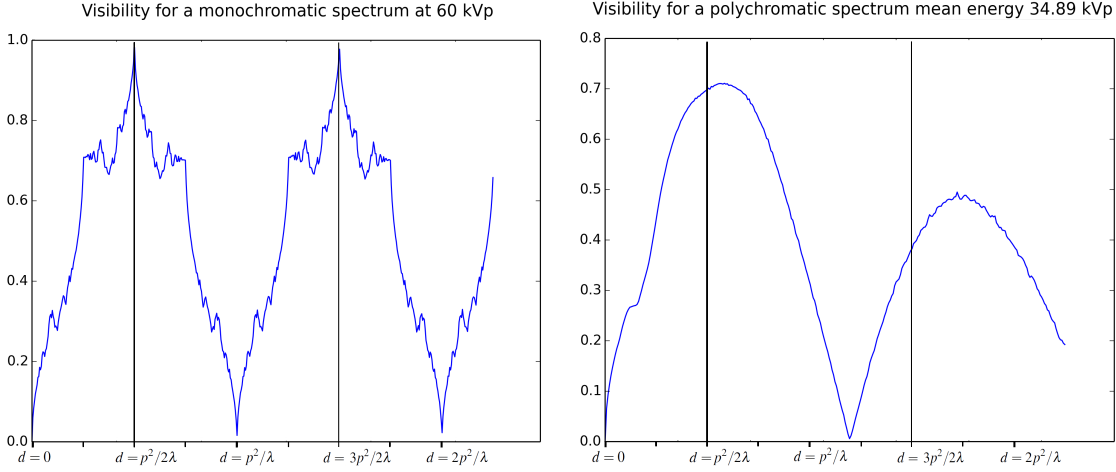


Figure 2.5: *Simulated visibility as a function of the Talbot-distance d_T , corresponding to the shown Talbot-carpets in Fig. 2.2. On the left side the visibility for a monochromatic source is shown. In accordance to theory the maximum is reached at odd fractional Talbot-distances. On the right side the visibility is smeared out and no sharp peaks occur, due to the fact of the loss of the monochromaticity of the beam. Nevertheless is the loss of visibility within a small distance a bigger disadvantage for conventional X-ray sources.*

the dependence on the distance between G_1 and G_2 , a fractional Talbot-distance with maximum visibility, e.g. $d = p^2/2\lambda$, can be substituted in the equation for the projected source size 2.19. Thus an equation for w as a function of the Talbot-distance and -order derives to:

$$w = S \times \frac{np_2^2}{2\lambda l} \stackrel{\frac{\lambda l}{S} = \zeta_s}{=} \frac{np_2^2}{2\zeta_s}, \quad (2.24)$$

where for the last step the coherence length ζ_s is substituted. With this relation the equation for the visibility can be rewritten as a function of the spatial coherence length

to [27]

$$V = e^{-(0.94np_2/\zeta_s)^2}, \text{ and thus again } \Rightarrow \zeta_s \geq \frac{0.94np_2}{\sqrt{\ln(V_0)}}. \quad (2.25)$$

Getting a feeling for the behaviour of this formulas for real experiments a few more numbers are introduced. As one can note on the left side of Fig. 2.2 the first order Talbot-distance occurs at $2,42m$, which is yet a big distance at normal labs, because the dimensions of the installations have to fit into a quite small hutch due to security requirements. For that reason higher Talbot orders $n > 1$ can be neglected because of space restrictions. The grating-period of the analyser grating used in general at this setup is $10\mu m$ and lets assume a required minimum visibility of $V_0 = 0.2$ then the required projected source size evolves to $w \leq 6.7\mu m$ or otherwise the transversal coherence length to $\zeta_s \geq 7.41\mu m$ from equations 2.23 and 2.25, respectively. These values are for a low required visibility quite small,yet and mostly far out of range for conventional source, but nevertheless as mentioned above is this technique applicable inducing the source grating.

Phase stepping routine: In the next short paragraph the phase stepping routine, where the defined relations above, especial Equ. 2.18 and 2.20 play an important rule is just explained in a brief manner, the reader more interested in detail see: [4, 10, 14]. What is done in this procedure is more or less explained in a few simple words: "Move one of the three gratings perpendicular to the beam direction and vertical to the grating lines, while holding the other two at fixed position, and record how the intensity pattern vary over different grating positions". Of course this is a very rude explanation, but this is more or less what has to happen retrieving phase information. (Again just one direction is taken into account, because in general depending on the bearing of the grating lines phase information is just required, if the stepping moves along the axis perpendicular to the grating layers.¹ Otherwise no information is recovered as one can imagine, because the pattern will not change due to the fact ,that there is no relative change between the distinct grating lines.) For a more precise explanation Equation 2.18 is rewritten in slightly different way, such that the intensity of every point x_d of the intensity pattern is expressed by

$$I(x_d, y = 0) = a_0 + a_1 \sin(\Phi_d + \varphi), \quad \text{with } \Phi_d = \frac{2\pi}{p_2} x_d, \quad (2.26)$$

with the offset a_0 , the amplitude a_1 and the corresponding transverse shift φ of the intensity distribution [3]. This equation contains the first two terms of a Fourier series and obviously solving this equation three different positions have to be measured, because for three unknown at least three different equations are needed. So the stepping has to exceed at least three steps getting feasible information and the stepping range should embrace one hole period of the analyser grating G_2 . Usually an odd number of stepping points is used, because a even number of sampling-steps causes no additional benefit.

¹As long as the gratings are perpendicular to the beam and the grating lines tend at the same direction, it does not matter in which direction, x- or y-direction or any other combination of them, the gratings are put into the beam.

Getting a good approach of the shape of the stepping-curve, the sampling rate over one period is extended to 7 steps for the case of this thesis, but there is no upper limit it is at least a trade off between better results and test-time. At each of this steps an intensity image is taken, meaning that the interference pattern is sampled in each detector pixel, which yields to a stepping-curve of the oscillating intensity describable with the equation above. Due to the fact that the focus of these procedure lies on the shift induced to the X-rays by the object which is illuminated, a reference stepping curve is recorded at the same stepping positions chosen for the object. With this two curves at hand three different imaging signals can be extracted at once from each pixel of the dataset as illustrated in Fig. 2.6 (a-c). Here the superscripted o and r denotes the object and reference frame, respectively:

- As depicted in Fig. 2.6 a), the attenuation of the object, which in general is referred to as AMP signal is:

$$a_0 = \frac{a_0^o}{a_0^r}. \quad (2.27)$$

This signal is equivalent to the conventional attenuation-based X-ray absorption imaging and relies also on the same physical principles.

- Fig. 2.6 b), shows the relative transverse shift of the interference pattern due to the angular refraction of the X-ray beam passing through the object. With equation 2.7 for the refracted angle and a given distance d between G_1 and G_2 and the period p_2 of the intensity distribution, the transverse shift is dependent on the differential phase shift of the wave-front as

$$\varphi = \frac{d\lambda}{p_2} \frac{\partial \Phi(x)}{\partial x}. \quad (2.28)$$

And the transverse shift of the stepping curve is given by

$$\varphi = \varphi^o - \varphi^r \quad (2.29)$$

There is likewise a abbreviation for this imaging signal known as Differential Phase Contrast (DPC)

- Analogue to equation 2.20 the visibility of the stepping curve can be defined as $V = a_1/a_0$, thus the relative visibility of the interference pattern becomes [16]

$$V = \frac{V^o}{V^r}. \quad (2.30)$$

The visibility in the object frame is reduced by the effect of small-angle scattering of the X-rays on sub-micron structures in the object, smaller than the pixel size, shown in Fig. 2.6 c). The general term for this imaging signal is X-ray Dark-field Imaging (DCI).

These three properties are called throughout the further chapters AMP, DPC and DCI projections. According to standard radiographic imaging the outcome of the different signals is the summation over the respective quantity along the beam direction across the object, which yields to two-dimensional projection images.

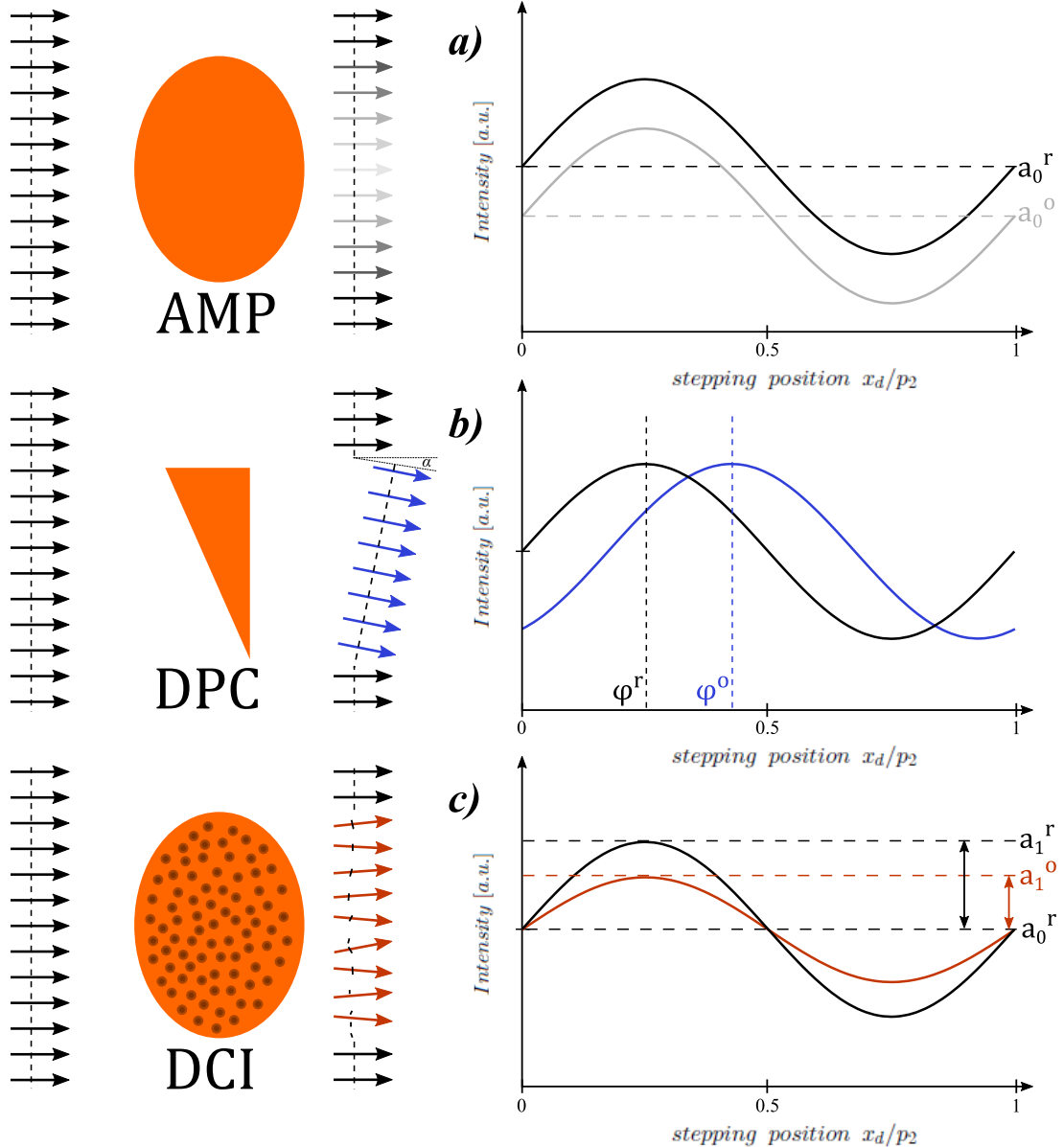


Figure 2.6: Resulting data output generated by the stepping procedure. The black solid line in the plots on the right side indicate the reference stepping curve, the coloured the curves including an object in the beam, respectively. a) the dashed lines indicate the respective mean intensity of the curve, so the decrease is proportional to the attenuation induced by the object. b) The transversal shift of the stepping curve is induced by a slightly deflection of the beam while passing through the object due to a differential phase shift of the incoming wave-front. c) due to random small angle-scattering on sub-pixel features of the object the amplitude of the resulting stepping-curve is reduced.

2.2.7 Magnification in curved wave geometry

In this small section a transition of the assumption of perfect plane waves in the latter sections, to a more real case of curved wave-fronts is described. By assuming a point like source the difference between the distance of source to object and source to detector, further denoted by SO and SD , respectively, induces a magnification factor of

$$M = \frac{SD}{SO}. \quad (2.31)$$

The geometrical considerations for this relation are shown in Fig. 2.7 for the case of an grating with a period p . The image of the grating on the detector is magnified by a factor M . This magnification factor obviously also has to be taken into account, installing the grating interferometer between source and detector, because the grating G_1 is then also treated as an object in te beam and thus also magnified. Staying at the treatment of the gratings as object, the interference fringes induced by G_1 also undergo the magnification and so the period changes from p_1 to Mg_1 . A way to avoid this, is producing periodic gratings which compensate this effect. Otherwise a mismatch of the exact distance between G_1 and G_2 results in Moire fringes at the detector declining the signal. As example a Moire fringe per 100 grating lines occurs for a magnification

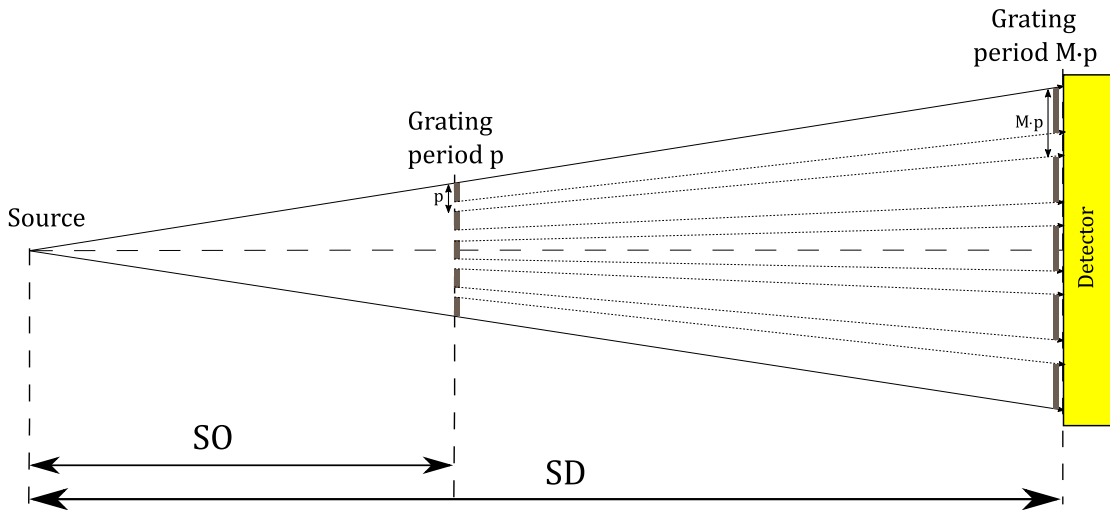


Figure 2.7: Geometric magnification in curved wave setups for a point like source. Depending on the position where the grating is placed in between source and detector the magnification factor varies form $\lim_{SO \rightarrow 0} M \rightarrow \infty$ right behind the source, to $\lim_{SO \rightarrow SD} M \rightarrow 1$ right in front of the detector.

differing just one percent from 1, and with a grating period $p_1 = 5 \mu\text{m}$ it ends up with 2 Moire fringes per millimetre. Nevertheless this factor also changes the Talbot distance, thus also the fractional Talbot distances used as distance between the two interferometer

gratings. The fractional Talbot distances given by equation 2.14 have also to be rescaled in the manner that [3]:

$$d_{T_{frac}} = M \frac{np^2}{8\lambda}. \quad (2.32)$$

So the consequence of this effect is, that the geometry of the setup has to be considered by the production of gratings, which means that the same grating is not categorically feasible for two different installations e.g. at one hand for a short setup in a lab and at the other hand at a synchrotron beam-line with a long geometry. In the next small part another effect, arising from curved wave fronts and thus magnification, is discussed with respect to a measurement technique for the spot size of the source.

2.2.8 Induced uncertainty by an expanded edge thickness at different magnifications

In the latter section the changes for the setup properties, arising by the transition from a ‘optimised hier muss ich noch das richtige wort finden’ system to a more ‘realistic’ system, were induced, but there are some more changes, which have to be accounted for a real system. As everybody can imaging, there is no real point source in nature, So every source however as small as they is has an expanded shape, which leads to complexity characterizing such a system. One example is the measurement of the extent of the source spot, using a so called knife edge. Therefore the knife edge, speaking o a very sharp edge of a small metal ashlar, which has been polished to be as smooth as possible, is put right in the centre of the beam. The exact procedure is described in chapter 5. In the following just the mismatch of this technique, with respect to the elongation of the edge in beam direction and the influence of the position of the ashlar speaking of the associated magnification, is considered. The structure for this is shown in Fig:???. Here denotes $S/2$ the half of the expanded source size, M_α and M_β the magnified image of the edge, whereby these two quantities differ from each other, corresponding to the thickness Δd of the ashlar and the angles α and β , which are dependent on the position of the cuboid and the spot-size of the source, varying from each other in the same way like M_α and M_β . For this case the tangent of α and β is given by:

$$\left. \begin{array}{l} \tan(\alpha) = \frac{S}{2d} = \frac{M_\alpha}{l-d} \\ \tan(\beta) = \frac{S}{2(d+\Delta d)} = \frac{M_\beta}{l-d-\Delta d} \end{array} \right\} \quad \frac{S}{2d} + \frac{S}{2(d+\Delta d)} = \frac{M_\alpha}{l-d} + \frac{M_\beta}{l-d-\Delta d}, \quad (2.33)$$

whereby the addition of both gives a relation between the spot size of the source and the magnified edge image resulting from the position between source and detector and the thickness of the ashlar. For the influence of the thickness Δd of the edge, just the equation for $\tan(\beta)$ is of interest, because just for this half of the relation the extend of the ashlar comes into play, assuming that the whole X-rays are absorbed by the cuboid. Getting a feeling for the contribution of the thickness Δd the right side of the relation from equation 2.33 for $\tan(\beta)$ is rewritten with the first two terms of the corresponding Taylor expansion around d and $(l - d)$, respectively, whereby the small variation is the

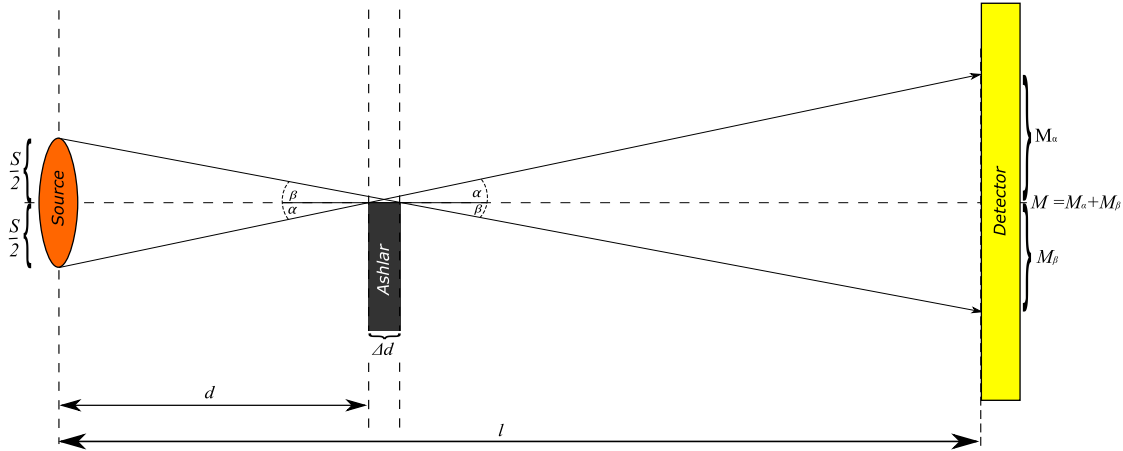


Figure 2.8: Sketch of the edge in the centre of the beam for the measurement of the source size. Due to the finite size of the edge in beam direction the upper half of the source produces a slightly smaller image of the edge on the detector-screen. This effect leads in reverse to a mismatch during the measurement of the size of the source.

thickness Δd . Thus $\tan(\beta)$ becomes:

$$\begin{aligned} \tan(\beta) &\approx \frac{S}{2d} - \frac{S}{2d^2} \underbrace{(d - d_0)}_{\hat{=} \Delta d} + \frac{S}{2d^3} \underbrace{(d - d_0)^2}_{\hat{=} \Delta d^2} \\ \text{subst: } (l-d) &= x \\ &\approx \frac{M_\beta}{x} - \frac{M_\beta}{x^2} \underbrace{(x - x_0)}_{\hat{=} \Delta d} + \frac{2M_\beta}{x^3} \underbrace{(x - x_0)^2}_{\hat{=} \Delta d^2}. \end{aligned} \quad (2.34)$$

As the focus lies on the contribution to the spot-size of the source, equation 2.33 is rearranged, so that the result is an expression for the source size :

$$S = \frac{d^3}{d^2 - \frac{d}{2}\Delta d + \Delta d^2} \left(\overbrace{\frac{M_\alpha + M_\beta}{x}}^M - \frac{M_\beta}{x^2} \Delta d + \frac{2M_\beta}{x^3} \Delta d^2 \right). \quad (2.35)$$

Getting a more manageable equation a substitution yields to

$$S = Ma - M_\beta(b - c), \quad (2.36)$$

whereby the substitutes a , b and c replace the pre factor of the respective M

$$a = \frac{d^3}{x(d^2 - \frac{d}{2}\Delta d + \Delta d^2)}, \quad b = \frac{d^3 \cdot \Delta d}{x^2(d^2 - \frac{d}{2}\Delta d + \Delta d^2)}, \quad c = \frac{2 \cdot d^3 \cdot \Delta d^2}{x^3(d^2 - \frac{d}{2}\Delta d + \Delta d^2)}. \quad (2.37)$$

As one can see is b and c a first and the second order term in Δd , respectively. Thus are these two the terms one is interested here, because the contribution to d^2 of $\Delta d \cdot d/2 + \Delta d^2$ is negligible. For $d = 0.5$ m and $\Delta d = 0.01$ m, which are quite big values for both, and a complete setup length of $l = 1.952$ m between source and detector, it is $\approx -2.4 \times 10^{-3}$, this yield to a value of $a = 0.35$ m. The setup- length l is never changed during the whole measurement just the position o the edge in between. Getting a lower and upper appraisal, lower and upper values for d , and Δd are introduced, which are used in the latter measurement as well. The limits for d are set to $d_{min} = 0.1$ m where the effect of the magnification is very strong ($M = \approx 19.52$) and $d_{max} = 0.5$ m. The thickness of the edge is never changed during the latter measurement, but at the first glance the focus lies on the influence of this property. So the limits for Δd are $\Delta d_{min} = 0.005$ m and $\Delta d_{max} = 0.01$ m. Here the subscripted *max* and *min* obviously denotes the maximal and minimal considered values. the different values of b , c and $(b - c)$ for different combinations of the limits are shown in Table:2.1. At the first glance it is obvious that just the influence of the first order-term b is yet very small. The contribution of the thickness Δd of the edge to this values has clearly a mathematical nature. Due to the small values the behaviour is strongly dependent on the enumerator, meaning that the half of the thickness halves the values for the linear term b and quarters them for the quadratic term c . Also One important aspect is, that the ashlar must have a distinct thickness, ensuring that as less as possible X-ray radiation passes through it, since in other respects the sharpness in the image of the edge is reduced, and thus it becomes harder to determine the true source size. The contribution of the distance d between edge and source however changes the value about one order of magnitude, so regardless

	d_{max}	Δd_{max}	d_{max}	Δd_{min}	d_{min}	Δd_{max}	d_{min}	Δd_{min}
limits [m]	0.5	0.01	0.5	0.005	0.1	0.01	0.1	0.005
b	2.4×10^{-3}		1.2×10^{-3}		3.0×10^{-4}		1.5×10^{-4}	
c	3.3×10^{-5}		8.2×10^{-6}		3.3×10^{-6}		8.1×10^{-7}	
$(b - c)$	2.4×10^{-3}		1.2×10^{-3}		3.0×10^{-4}		1.5×10^{-4}	

Table 2.1: *Results for the mismatch due to a finite edge thickness Δd and different magnifications. In accordance with mathematical relations the contribution of Δd to the values is strongly enumerator dependent, hence the small values. The second order pre factor term is always two times smaller than the first order pre factor term and thus negligible (No change of the value adding first and second order terms). Due to the small values of the first order pre factor which is always of the order $\leq 10^{-3}$ the effect on the precision of the measurement can be ignored, since effects of misalignments of the edge deliver a much higher contribution.*

of how thick the edge is the contribution of the magnification is higher of course just up to a distinct extent of the thickness, but no one would use a edge with a thickness of a few centimetres just because of difficulties aligning the edge perpendicular to the beam direction. The result of this evaluation is that the contribution of the thickness of the edge is negligible over a broad area, because even considering a unrealistic thickness of $\Delta d = 10$ cm the pre factor b is just ≈ 0.05 . On the other side due to the bigger contribution of the magnification in this case it is more important insuring a preferably perpendicular alignment of the edge with respect to the beam direction, because a slight tilt of the edge induces a big smear o the image of the edge.

2.3 Spatial system response

In this section a short introduction to linear system theory is presented, focussing on the characterization of imaging systems. For a detailed insight the reader is referred to [6, 7, 19, 24, 25]. Here, only the basic quantities for real and radially symmetric response functions, representing the experimental, which is characterized, are treated.

2.3.1 Real- and frequency-space response functions

Linear system theory is a common approach describing the spatial properties of imaging systems. The applicability of the superposition principle on an imaging system implies it's linearity, meaning the response to a linear combination of incitements, generally called input signals, is the same linear combination of the particular responses, called output signals. Assuming that the response of the linear system is also shift invariant, i.e. the system is linear and shift invariant (LSI), the output can be calculated by convolution:

$$I(x, y) = S(x, y) \otimes O(x, y) = \int_{-\infty}^{\infty} \int_{-\infty}^{\infty} S(x - x', y - y') O(x', y') dx' dy', \quad (2.38)$$

$I(x, y)$ is the measured image, $s(x, y)$ is the point spread function Point-spread-function (PSF), $o(x, y)$ describes the object, and \otimes designates the two-dimensional convolution operator. Because of dealing with intensities, all functions in real space are real functions, therefore the PSF is defined to be normalized to unity, i.e.:

$$\int_{-\infty}^{\infty} \int_{-\infty}^{\infty} S(x, y) dx dy = 1. \quad (2.39)$$

For a full characterization of the spatial system response of a system, the measurement of the PSF or the appropriate Modulation transfer function (MTF) is absolute. The big advantage knowing these properties, is that they can be used correcting blur and other artefacts via deconvolution techniques. Since the PSF is the response of the system to a delta-peak shaped input signal, in other words the description of an image produced by a point-like source, which is inaccessible in real life, the PSF has to be derived indirectly from objects with well known structure like edges or slits. The related MTF can be expressed using the convolution theorem, stating that the convolution of two functions

in real space is just a multiplication in Fourier space. Hence equation 2.38 becomes using convolution and Fourier transform

$$\mathcal{F}(I(x, y)) = \mathcal{F}(S(x, y)) \cdot \mathcal{F}(o(x, y)) \Rightarrow \tilde{I}(u, v) = \tilde{S}(u, v) \cdot \tilde{O}(u, v), \quad (2.40)$$

where the letters with tilde indicate the respective Fourier transformed function. The so called Optical transfer function (OTF) is the Fourier transform of the Point-spread-function $\tilde{S}(u, v)$ and is in general a complex function, but can be split in phase and amplitude such as

$$\tilde{S}(u, v) = M(u, v)e^{i\Psi(u, v)}, \quad (2.41)$$

with the Phase transfer function (PTF) $\Psi(u, v)$ and the so called Modulation transfer function of the system, related in a manner that

$$M(u, v) = \frac{|\tilde{S}(u, v)|}{\tilde{S}(0, 0)} = |\tilde{S}(u, v)| \quad (2.42)$$

is the absolute value of the the OTF. This quantity correlates also with the reduction of contrast of an sinusoidal signal comparable to part 2.2.6. In general the PSF is assumed to be radial symmetric, thus a one-dimensional description in polar coordinates is possible. Using this approach also the OTF is radial symmetric and thus real, which reduces equation 2.41 to $\tilde{S}(w) = M(w)$ (whereby this is the polar coordinate representation which is still two-dimensional!). As consequence the system response can also be fully described by the MTF for this assumptions [7]. Now in the following sections the required mathematical armamentarium for the evaluation of the PSF from easy structured images is presented in a short manner.

2.3.2 Edge- and Line- spread function (ESF/LSF)

The spatial system response on an edge-shaped input signal is generally defined as the Edge spread function (ESF). On the other hand is the Line-spread-function (LSF) obviously the response on a line shaped signal. These functions are both two-dimensional functions, but with a constant behaviour along the direction parallel to the edge or rather line. According to this both can be expressed by a one-dimensional representation. In the further it is shown that the LSF is the first derivative of the ESF as well as the projection of the PSF. Considering that both objects are parallel to the y-axis, both functions are independent of y. Thus the Line-spread-function is defined as(using equation 2.38) [7]:

$$LSF(x) = \int_{-\infty}^{\infty} \int_{-\infty}^{\infty} S(x - x', y - y') \delta(x') dx' dy' = \int_{-\infty}^{\infty} S(x, y') dy', \quad (2.43)$$

with the Point-spread-function $S(x, y)$ defined in section 2.3.1 and the Dirac- delta function $\delta(x)$ describing the line object $O_l(x, y)$ parallel to the y-axis, which is unity integrated from $-\infty$ to ∞ . Thus the projection of the Point-spread-function in y direction is

equal to the $LSF(x)$. In contrast the edge object $O_e(x, y)$ with the same constraints can be written as:

$$O_e(x, y) = O_e(x) = \begin{cases} 0 & \text{for } x \leq 0 \\ 1 & \text{else.} \end{cases} \quad (2.44)$$

Thus the ESF is given by [7]:

$$\begin{aligned} ESF(x) &= \int_{-\infty}^{\infty} \int_{-\infty}^{\infty} S(x - x', y - y') O_e(x') dx' dy' \\ &= \int_{-\infty}^{\infty} O_e(x') \int_{-\infty}^{\infty} S(x - x', y - y') \delta(x') dy' dx' = O_e(x) * LSF(x), \end{aligned} \quad (2.45)$$

here $*$ denotes the one-dimensional convolution and $O_e(x)$ denotes the function for the edge shaped object defined above. So the derivative of the ESF appears to be:

$$\frac{d}{dx} ESF(x) = \frac{d}{dx} \{O_e(x) * LSF(x)\} = \delta(x) * LSF(x) = LSF(x). \quad (2.46)$$

This equation holds because again convolution theory states, that the derivative of a convolution of two functions can be rewritten as the convolution of the derivative of one of the two functions with the other function or the other way round. In addition the derivative of the edge function results in the delta function, thus consequential the derivative of the ESF yield to the LSF.

Furthermore it is possible to generalize the above defined relation, in order that the orientation of the edges or lines can be arbitrary only with one constraint, they have to pass through the coordinate origin. With that at hand it is possible to determine the two-dimensional PSF $S(x, y)$, using tomographic reconstruction techniques for edge projections with different angles. By assuming a radial symmetric Point-spread-function the Edge spread function (ESF) is independent of the projection angle and one edge is sufficient describing the full PSF. For further reading see [7].

2.3.3 PSF of a complex system

The former section describes the evaluation for the Point-spread-function (PSF) using edge or line objects. Now the determination of the PSF of a whole system is a very challenging problem, because each part e.g. source or detector of an imaging system has his own two-dimensional PSF. It is one problem to determine the Point-spread-function (PSF) of the whole system, but measuring this property is just one step towards the quantities, which are rather expected. The PSF of an simple imaging system, consisting just of source and detector, is given by convolution of the respective PSF's

$$PSF_{System} = PSF_{Source} \otimes PSF_{Detector} = \mathcal{F}^{-1}[\mathcal{F}(PSF_{Source}) \cdot \mathcal{F}(PSF_{Detector})], \quad (2.47)$$

whereby the last part of the equation is just the first part, but rewritten in Fourier transforms to simplify the further explanations. In general one has to deal with a curved wave setup as explained in 2.2.7, thus due to geometrical thoughts one has to account

the magnification in the latter equation, because the PSF of the source is spread out over the detector screen by this magnification factor. For convenience a one-dimensional behaviour is assumed for the further steps. Normally for X-ray sources a Gaussian shaped PSF is assumed, whereby the sigma (equal to the width of the function) of the Gaussian has to be multiplied by the magnification factor minus one, thus equation 2.47 is rewritten with Gaussian functions for the respective parts such that:

$$A_{System} e^{-\frac{1}{2}(\frac{x-b}{\sigma_{System}})^2} = \mathcal{F}^{-1}[\mathcal{F}(A_{Source} e^{-\frac{1}{2}(\frac{x-b}{\sigma_s \cdot (M-1)})^2}) \cdot \mathcal{F}(A_{Detector} e^{-\frac{1}{2}(\frac{x-b}{\sigma_d})^2})], \quad (2.48)$$

with the amplitudes A_{System} , A_{Source} and $A_{Detector}$ and sigma's σ_{System} , σ_s and σ_d for the different parts, respectively. The solution of this equation is straight forward, because the Fourier transform of a Gaussian is again a Gaussian, but with reciprocal width σ . With this equation at hand it is possible to determine the PSF of the source, by knowing the PSF of the detector, and thus the spot-size of the source which is generally defined as the FWHM of this function. Hence the focus lies on the evaluation of the size of the source, special attention has to be given to the width of the respective Gaussian. For that reason some assumptions are made reaching this aim in a more easy way. Firstly the amplitudes are set to one and the offset b is set to zero, so the peak is centred around the origin. Then both sides are multiplied by the natural logarithmic function \ln getting rid of the exponential, so this yields to:

$$-\frac{1}{2} \left(\frac{x}{\sigma_{System}} \right)^2 = -\frac{1}{2} \left(\frac{x}{\sigma_s \cdot (M-1)} \right)^2 - \frac{1}{2} \left(\frac{x}{\sigma_d} \right)^2. \quad (2.49)$$

After cancelling out the pre factors and the x -es the equation simplifies to:

$$\left(\frac{1}{\sigma_{System}} \right)^2 = \left(\frac{1}{\sigma_{source} \cdot (M-1)} \right)^2 + \left(\frac{1}{\sigma_{detector}} \right)^2. \quad (2.50)$$

Inverting of the hole equation and taking the square-root the final equation for the system's spread width is given by:

$$\sigma_{System} = \sqrt{\sigma_{source}^2 \cdot (M-1)^2 + \sigma_{detector}^2}. \quad (2.51)$$

With this equation at hand it is now possible to determine the properties of a system at the spatial- and of course if needed at the frequency- domain.

3 The Setup

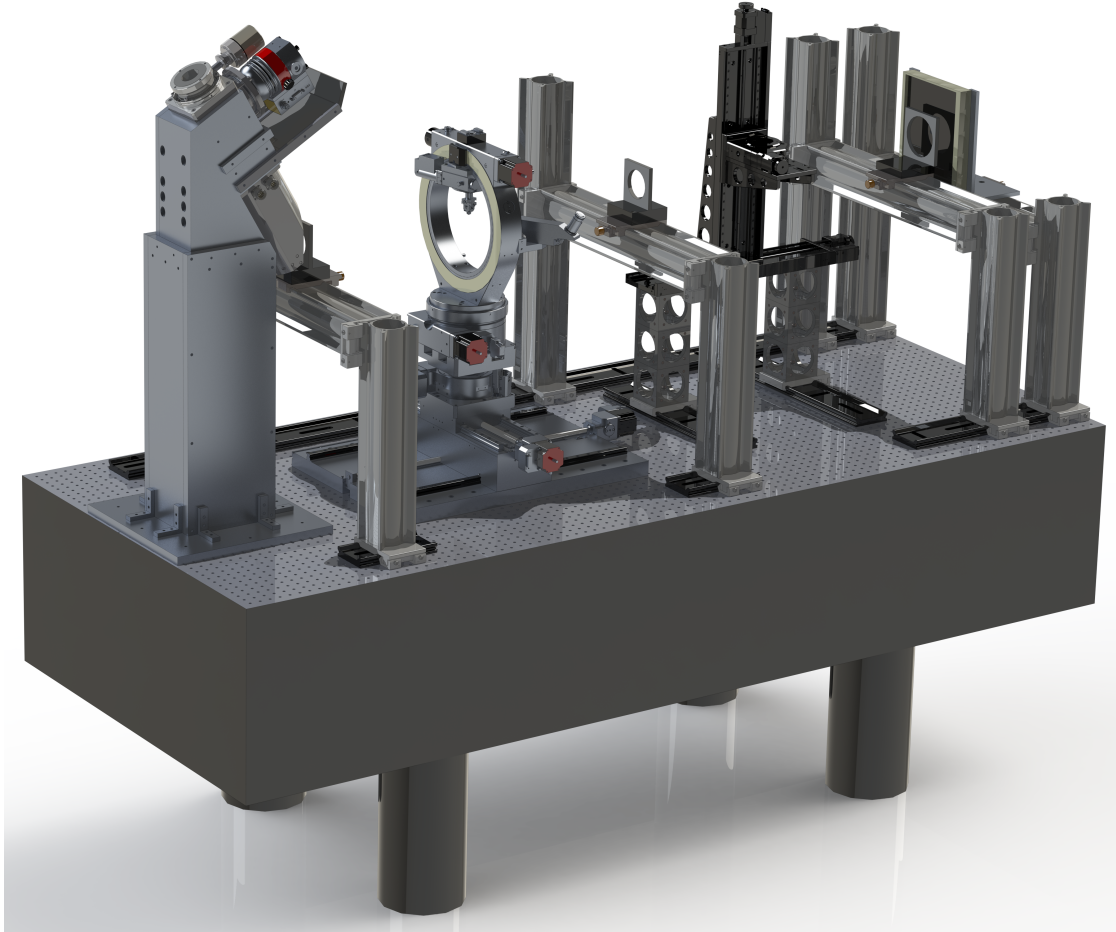


Figure 3.1: *Rendering of the setup which is characterized in this thesis. the optical table has a size of $2.4 \text{ m} \times 1 \text{ m}$. On the left side the micro-focus X-ray tube and on the other side of the table the Varian X-ray detector is mounted, which is usually used for clinical applications. In-between the important part of this setup the grating interferometer with stages between the gratings, handling the samples during the measurements, is placed.* (source: Friedrich Prade)

In this chapter a short introduction is given, about the individual parts and their properties of the setup. The setup was built up in administration of the biomedical physics

group e17, by Friedrich Prade and Florian Schaff. The whole setup consists more or less of three main parts, Source, Interferometer and Detector. The general structure is depicted in Fig:3.1. The micro-focus source is placed on the left and the X-ray detector on the right side. In-between the part, which needs the most space and where the ‘physics’ happens, is mounted. Right in front of the Detector the analyser grating G_2 is attached on its own bench, in the middle of the table the phase grating G_1 is also placed on a bench, and right in front of the source the so called source grating G_0 is mounted. All gratings are preferably aligned perpendicular to the beam direction and with the same orientation of the grating-lines to each other, avoiding shadowing and that Moire-fringes show up. Between the gratings two different stages are placed handling the samples during the measurement, which can be controlled fully automatic, thus computer tomography measurements without interrupting the procedure are possible. In the next three sections the different parts are highlighted in a more detailed way, starting at the very beginning, the production of X-rays at the source, followed by the interacting part within the interferometer and at least the creation of the images at the detector.

3.1 The source

The most indispensable part is of course the production of the required radiation itself. At this setup a so called ‘micro-focus’ X-ray tube designed and crafted by ‘X-RAY WorX GmbH’ is used, which provides some big improvements compared to commercial X-ray sources used for clinical applications, especially at the area of resolution restraints. The structure is in general like the structure of a conventional x-ray tube, but with additional parts e.g. an electron optic influencing the direction of the electrons generated by the cathode. For a complete overview of the properties and drawings of micro-focus tubes provided by this company see [28, 29, 30, 31].

3.1.1 Dimensions and structure

The dimension and structure of the source differs just in the additional parts from conventional sources. It consists of a cathode filament heated by a high voltage power supply generating a electron beam, which is accelerated due to a electromagnetic field between cathode and anode, to the other end of the tube hitting a tungsten reflection target, which finally produces the X-ray radiation. In-between of these two main parts a additional part,a so called electron optic is placed. It consists of several magnetic coils which influences the trajectory of the electron beam. Four coils are responsible for the deflection of the whole beam in both x and y direction. The other coils are used focussing the electron beam, which is in general spread over a large area, to a very tiny area improving the resolution strength of the whole setup. A drawing of the dimension of the source and the electron optic in detail is shown in Fig. 3.2. Using such a focussing equipment, it is inevitable to evacuate the whole tube avoiding flash-overs between filament and target. This is possible,because due to the strong compression of the particular electrons in the beam a ‘electron bridge’ guiding current from cathode

to anode can arise. Therefore in addition a vacuum turbo pump is mounted on top of the tube, providing a vacuum of the order of 4×10^{-6} schaun welche einheit und größerenordnung avoiding such flash-overs. As in conventional sources just about one percent of the electrons hitting the target, produces X-ray radiation. The remaining part heats the anode material. Thus especial for the case of a focussing source a cooling of the target is needed, avoiding that the target material melts down.

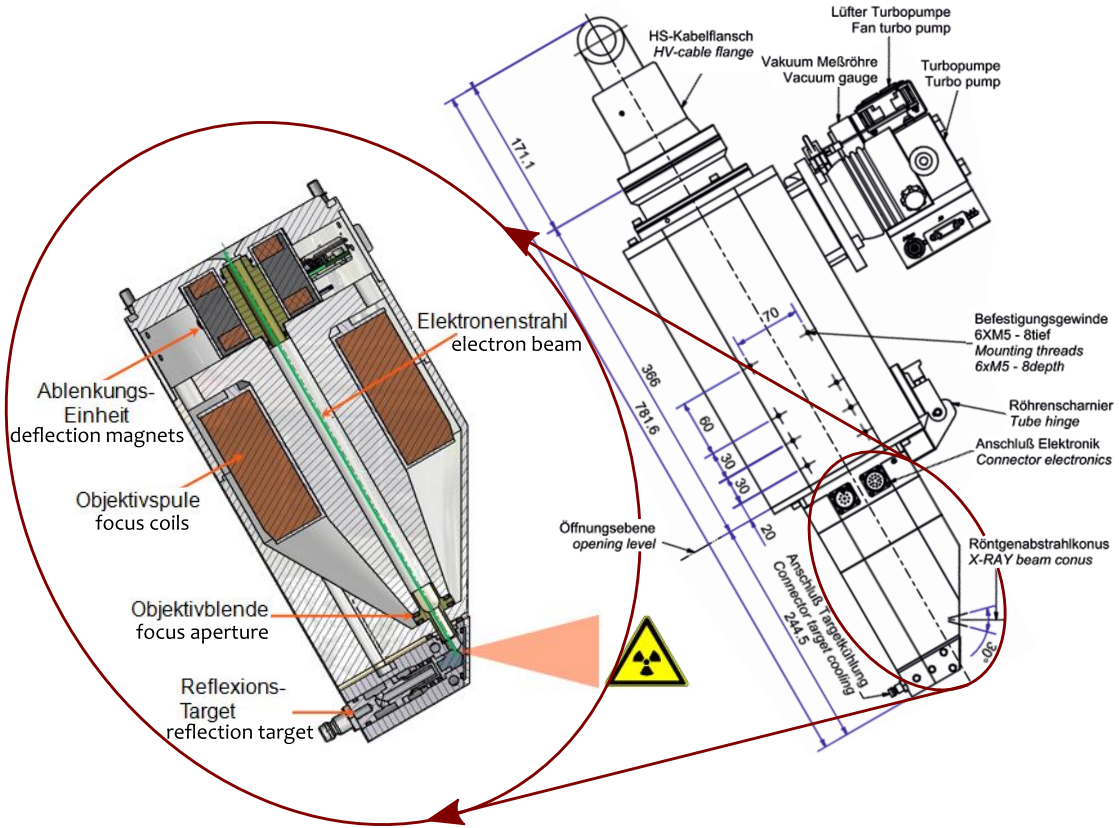


Figure 3.2: Dimensions of the source and its components. The part highlighted in the red circle shows the focussing electron-objective, which improves the resolution due to the fact scaling the spot size down to the micron range. (source: ©X-RAY WorX GmbH 2015 <http://www.x-ray-worx.com>)

3.1.2 properties

In difference to conventional X-ray tubes this tube is working over at broad tunable range from 20 kV up to 160 kV, but due to the design energy of the Talbot-Lau interferometer it operates in general at 60 kV. Depending on the adjusted acceleration voltage the power-output ranges from 1 W up to 300 W. The construction of the tube offers a almost infinite lifetime, because the filament, which is the only thing which usually breaks down, can

be easily changed, thanks to its ‘open’ architecture (see Fig.3.2 right behind the opening level the filament holder is mounted). Another advantage compared to conventional sources with a spot size of $\approx 2 \text{ mm}^2$ is that the spot size of this source is reduced down to the micron range. Hence the spatial resolution is strongly improved, why it is possible resolving features down to sizes of $\approx 2 \mu\text{m}$ [31]. With the X-COM software [30] also developed and traded by X-RAY WorX several adjustments are possible. One example for an additional feature is the possibility to ‘stepp’ the beam in both x or y direction thanks to the linkage of the deflection magnets. With this feature a transition from a mechanical stepping procedure to a ‘magneto-stepping’ for the phase contrast technique comes into range, which provides several advantages e.g. prevention of grating vibrations during the stepping process.

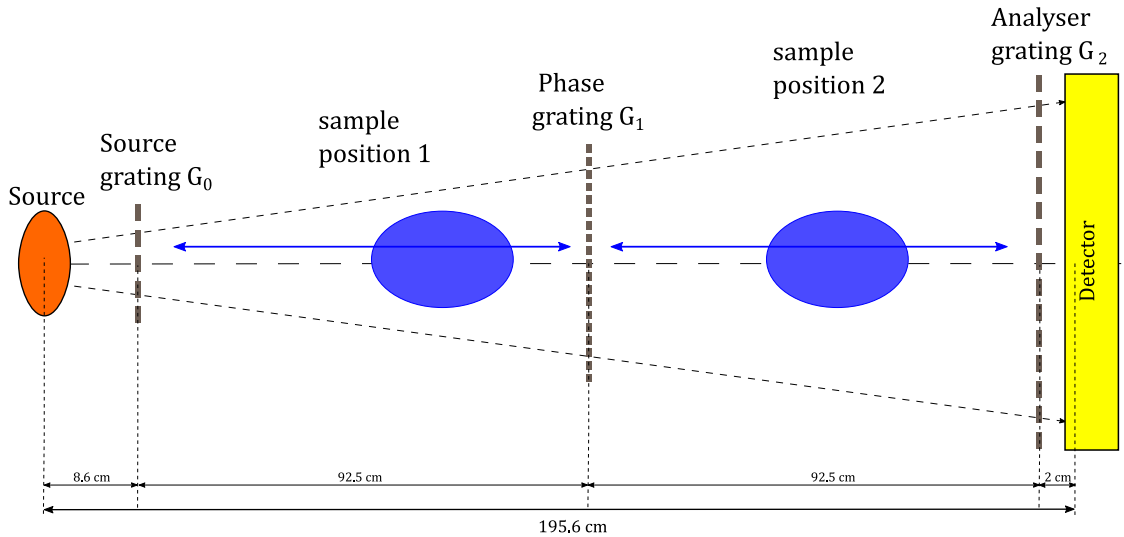


Figure 3.3: Drawing of the relative distances in-between the setup and different sample positions. This drawing shows a symmetric setting of the gratings, thus the magnification factor is 2 and the analyser grating has twice the periodicity as the $\pi/2$ phase grating. The gratings are also arranged to operate at the first fractional Talbot distance. The blue extended arrows indicate the possible positions for the sample between the gratings.

3.2 Sample handling between the gratings

As depicted in Fig.3.3, the Talbot-Lau interferometer itself captures the main part of the setup length, starting about eight cm behind the source, with the source grating G_0 , which is an absorption type with a grating period of $10 \mu\text{m}$ and a height of $??$. At the other side just two cm in front of the flat-panel detector the analyser grating G_2 with the same periodicity of $10 \mu\text{m}$ as G_0 and a grating height of $170 \mu\text{m}?????m$, thus also an absorption grating, is placed. Due to the high absorbency and the easy handling

these two gratings are made of gold as described in 2.2.4. Accounting the magnification factor of two for a symmetric setup, the phase grating G_1 with a periodicity of $5 \mu m$ and a nickel height of ??????? has to be put right in the middle between the other gratings so the distance between the gratings is generally $92.5 cm$, respectively. The gratings are not set arbitrarily to these distances, but they are put there on purpose, accounting the first fractional Talbot distance for a design energy of $45 keV$. In-between the gratings two different kinds of sample holders are placed with different properties. The first one between G_0 and G_1 is an Euler cradle. the main advantage of this stage is, that the sample can be rotated around its own axis and furthermore rotated around the beam axis as well. The second stage is a usual tomography stage which is put between G_1 and G_2 . Depending on the expected results and the sample is put on one of these two stages. So as example if a bigger magnification is needed resolving small detail within a sample the Euler cradle is recommended. On the other hand if one is interested in the induced phase shift one has to assure to get close to the phase grating, because the sensitivity enhances getting closer to it. But for this case both stages are feasible, because it makes no difference if the sample is placed in front or behind the phase grating.

3.3 detector properties

The detector used for imaging is a PaxScan 2520DX digital flat-panel detector generally used for dental cases. The detector is developed and traded by Varian medical systems and is based on amorphous silicon technology with Caesium Iodine (CsI) as conversion material on top. The main advantage of this material are radiation hardness $> 1Mrad$, a broad input energy range from about $40 - 160kVp$, good low dose performance, immunity for single photon events within the substrate and proven 3-D soft tissue capability. The total pixel area is $19.5 \times 24.4cm$ with a pixel size of $127 \mu m^2$ this yields in 1536×1920 pixel. The limiting resolution is stated to be $3.94lp/mm$ or in other words $253.81\mu m$ in both x- and y-direction [21]. A picture of the detector is shown in Fig.???. For reasons of protection a $2.5mm$ thick carbon fibre plate combined with aluminium is placed in front of the active detector area. Right behind this plate the active crystal layer with $\approx 9mm$ thickness is placed.

4 Time- and power- stability of the X-ray tube

The following chapter contains a characterization of the time- and power stability properties of the source. These qualities are elemental getting a feeling about the performance of the source. For example a fluctuation in the radiation-output during a measurement can destroy the whole outcome, because e.g. a correction with a flatfield does not properly cancel out the influence of the spectrum during the measurement.

4.1 Time-stability

4.1.1 Comparison of the stability over different time periods

4.2 Power-stability

5 Characterization of the spatial system response

6 Spectra measurements

7 Comparison of different grating interferometer constellations

8 summary and outlook

List of Figures

2.1	Attenuation and phase shift of electromagnetic waves	4
2.2	Simulated Talbot-carpets for a grating with a duty cycle of 0.5 a phase shift of $\pi/2$ and a grating period of $5\mu m$	8
2.3	Sketch of a Talbot-Lau interferometer	10
2.4	Different types of deep micro-structured gratings used for X-ray interferometry	11
2.5	Simulated visibility as function of Talbot-distance d_T	13
2.6	Resulting data output generated by the stepping procedure.	16
2.7	Geometric magnification in curved wave setups	17
2.8	Drawing of the edge in the centre of the beam for the measurement of the source size	19
3.1	Rendering of the whole setup	25
3.2	Dimensions of the source with focussing system	27
3.3	Drawing of the relative distances between the particular parts of the setup	28

List of Tables

2.1	Results for the mismatch due to a finite edge thickness Δd at different magnifications	20
-----	--	----

Acronyms

AMP Signal of the Amplitude modulation. 15

DCI Dark-field Imaging. 15

DPC Differential Phase Contrast. 15

ESF Edge spread function. 22, 23

FWHM full width at half maximum. 12, 24

LSF Line-spread-function. 22, 23

LSI linear and shift invariant. 21

MTF Modulation transfer function. 21, 22

OTF Optical transfer function. 22

PSF Point-spread-function. 21–24

PTF Phase transfer function. 22

Bibliography

- [1] ALS-NIELSEN, Jens: *Elements of Modern X-ray Physics*. Second Edi. A John Wiley & Sons, 2011. – ISBN 9780470973950
- [2] AMPTEC INC.: *Datasheet XR-100T-CdTe*
- [3] BECH, Martin: *PhD Thesis X-ray imaging with a grating interferometer*, University of Copenhagen Denmark, Dissertation, 2009. – 173 S
- [4] CREATHE, Katherine: V Phase-Measurement Interferometry Techniques. In: *Progress in Optics* 26 (1988), Nr. C, S. 349–393. – ISBN 0079-6638
- [5] CREMER, Jay Theodore J.: *Neutron and X-ray Optics, Jay Theodore Cremer, Jr., Elsevier, 2013.pdf*. First Edit. 2013. – 1124 S. – ISBN 9780124071599
- [6] CUNNINGHAM, I a. ; FENSTER, a: *A method for modulation transfer function determination from edge profiles with correction for finite-element differentiation.*
- [7] DONATH, Tilman: Quantitative X-ray Microtomography with Synchrotron Radiation. (2007), S. 209
- [8] KÖHLER, Jörg: Der Talbot-Effekt / Universität Regensburg, Institut für Experimentelle und Angewandte Physik. 2008. – Forschungsbericht. – 1–12 S
- [9] LEI, Yaohu ; DU, Yang ; LI, Ji ; ZHAO, Zhigang ; LIU, Xin ; GUO, Jinchuan ; NIU, Hanben: Fabrication of x-ray absorption gratings via micro-casting for grating-based phase contrast imaging. In: *Journal of Micromechanics and Microengineering* 24 (2014), Nr. 1, S. 015007. – URL <http://stacks.iop.org/0960-1317/24/i=1/a=015007?key=crossref.c8d5bae0afdef4852a68c7fb41ef568e>. – ISSN 0960-1317
- [10] LEWIS, Andrew J.: *Absolute length measurement using interferometry*, UNIVERSITY OF LONDON, IMPERIAL COLLEGE OF SCIENCE, TECHNOLOGY AND MEDICINE, 2002. – 324 S
- [11] LI, Ke ; ZAMBELLI, Joseph ; BEVINS, Nicholas ; GE, Yongshuai ; CHEN, Guang-Hong: Spatial resolution characterization of differential phase contrast CT systems via modulation transfer function (MTF) measurements. In: *Physics in medicine and biology* 58 (2013), Nr. 12, S. 4119–35. – URL <http://www.ncbi.nlm.nih.gov/pmc/articles/PMC3746757/> (Linking) – ISBN 1361-6560 (Electronic) 0031-9155 (Linking)

- [12] LI, Ke ; ZAMBELLI, Joseph ; BEVINS, Nicholas ; GE, Yongshuai ; CHEN, Guang-Hong: Spatial resolution characterization of differential phase contrast CT systems via modulation transfer function (MTF) measurements. In: *Physics in medicine and biology* 58 (2013), Nr. 12, S. 4119–35. – URL <http://www.ncbi.nlm.nih.gov/pmc/articles/PMC3746757/> – ISBN 1361-6560 (Electronic) 0031-9155 (Linking)
- [13] LIU, Huiqiang ; WU, Xiseng: Optimization of reconstructed quality of hard x-ray phase microtomography. 54 (2015), Nr. 18, S. 5610–5618
- [14] MOMOSE, Atsushi: Recent Advances in X-ray Phase Imaging. In: *Japanese Journal of Applied Physics* 44 (2005), Nr. 9A, S. 6355–6367. – ISBN 0021-4922
- [15] MUELLER, Mark: Experimental characterization of the first preclinical X-ray phase contrast CT scanner. (2013)
- [16] PFEIFFER, F ; BECH, M ; BUNK, O ; KRAFT, P ; EIKENBERRY, E F. ; BRÖNNIMANN, Ch ; GRÜNZWEIG, C ; DAVID, C: Hard-X-ray dark-field imaging using a grating interferometer. In: *Nature materials* 7 (2008), Nr. 2, S. 134–137. – ISBN 1476-1122
- [17] PFEIFFER, Franz ; WEITKAMP, Timm ; BUNK, Oliver ; DAVID, Christian: Phase retrieval and differential phase-contrast imaging with low-brilliance X-ray sources. In: *Nature Physics* 2 (2006), Nr. 4, S. 258–261. – ISBN 1745-2473
- [18] PFEIFFER, Franz ; WEITKAMP, Timm ; DAVID, Christian: X-ray phase contrast imaging using a grating interferometer. In: *Europhysics News* 37 (2006), Nr. 5, S. 13–15. – ISSN 0531-7479
- [19] SAMEI, E ; FLYNN, M J. ; REIMANN, D a.: A method for measuring the presampled MTF of digital radiographic systems using an edge test device. In: *Medical physics* 25 (1998), Nr. 1, S. 102–113. – ISBN 0094-2405 (Print) 0094-2405 (Linking)
- [20] SCIENTIFIC CROSSROADS ; AMPTEC INC.: X R F F P S o f t w a r e G u i d e V.3.30. (2008)
- [21] SYSTEMS, Varian medical: *PaxScan ® 2520DX Digital Image Receptor*
- [22] TALBOT, Henry F.: Facts relating to Optical Science. In: *Philosophical Magazine and Journal of science* (1836)
- [23] VAN DER VEEN, Friso ; PFEIFFER, Franz: Coherent x-ray scattering. In: *Journal of Physics: Condensed Matter* 16 (2004), Nr. 28, S. 5003–5030. – ISBN 0953-8984\1361-648X
- [24] WAGNER, Robert F.: Toward a unified view of radiological imaging systems. In: *Medical Physics* 1 (1974), Nr. 1, S. 11. – ISSN 00942405

- [25] WAGNER, Robert F.: Toward a unified view of radiological imaging systems. Part II: Noisy images. In: *Medical Physics* 4 (1977), Nr. 4, S. 279. – ISBN doi:10.1118/1.594362
- [26] WEITKAMP, Timm ; DAVID, Christian ; PFEIFFER, Franz: Tomography with grating interferometers at low-brilliance sources. (2006)
- [27] WEITKAMP, Timm ; DIAZ, Ana ; DAVID, Christian ; PFEIFFER, Franz ; STAM-PANONI, Marco ; CLOETENS, Peter ; ZIEGLER, Eric: X-ray phase imaging with a grating interferometer. In: *Optics express* 13 (2005), Nr. 16, S. 6296–6304. – ISBN 1094-4087
- [28] X-RAY WORKX GMBH: *CAD Drawings XWT-160-SE (1 : 5)*
- [29] X-RAY WORKX GMBH: *DATASHEET*. 2013
- [30] X-RAY WORKX GMBH: *X-COM software manual*. 2013
- [31] X-RAY WORKX GMBH: *MICROFOCUS X-RAY TUBES PRODUCT LINE SE*. 2015
- [32] XIN, Liu ; JIN-CHUAN, Guo ; XIANG, Peng ; HAN-BEN, Niu: Visibility in differential phase-contrast imaging with partial coherence source. In: *Chinese Physics* 16 (2007), Nr. 6, S. 1632–1636. – ISBN 1009-1963

